Epistemic uncertainty in California-wide synthetic seismicity simulations

April 10, 2011

Fred F. Pollitz[1]

[1] *USGS, Menlo Park, CA, USA;*

Abstract

Generation of seismicity catalogs on synthetic fault networks holds promise for providing key inputs into probabilistic seismic hazard analysis, e.g. coefficient of variation, mean recurrence time as a function of magnitude, probability of fault-to-fault ruptures, and conditional probabilities for foreshock-mainshock triggering. I employ a seismicity simulator that includes the following ingredients: static stress transfer, viscoelastic relaxation of the lower crust and mantle, and vertical stratification of elastic and viscoelastic material properties. A cascade mechanism combined with a simple Coulomb failure criterion, is used to determine the initiation, propagation, and termination of synthetic ruptures. It is employed on a 3D fault network provided by Steve Ward for the SCEC Earthquake Simulators Group. This California fault network, initially consisting of 8000 patches, each of $\sim$ 12 square km size,

has been re-discretized into ~ 100000 patches, each of ~ 1 square km size, in order to simulate the evolution of California seismicity and crustal stress at magnitude M$\sim 5-8$. Resulting synthetic seismicity catalogs spanning 30000 years and about one-half million events are evaluated with magnitude-frequency and magnitude-area statistics. For a-priori choices of fault slip rates and mean stress drops, I explore the sensitivity of various model constructs on input parameters, particularly mantle viscosity. Slip maps obtained for the southern San Andreas fault show that the ability of segment boundaries to inhibit slip across the boundaries (e.g., to prevent multi-segment ruptures) is systematically affected by mantle viscosity.

1 Introduction

Seismicity in Earth's crust is governed by numerous physical processes that shape the crustal stress field at a variety of spatial scales as well as local conditions on the causative faults (e.g. Shaw and Rice, 2000; Lapusta et al., 2000; Fitzenz and Miller, 2004; Harris, 2004; Ben-Zion, 2008). These include, at the microscopic scale, fault zone rheology and poroelasticity, and, at the macroscopic scale, elasticity of the upper crust and ductile rheologies of the lower crust and upper mantle. A complete understanding of earthquake occurrence would require the assimilation of these processes over a wide range of spatial and temporal scales, a goal which is not attainable in the near future. The statistics of large eathquake occurrence, however, may be simpler to analyze because they may be thought of as culminating events in the macroscopic processes of tectonic strain accumulation and release

(e.g. Robinson and Benites, 1995, 1996; Ward, 2000; Rundle et al., 2002; Ben-Zion et al., 2003; Rundle et al., 2004). On synthetic fault networks, rich spatio-temporal patterns of seismicity result from the simple process of elastic stress transfer, and that process alone may drive the overall statistics in more sophisticated models (Rundle et al., 2004).

Computer simulations that incorporate a portion of the physics needed to describe earthquakes have illuminated the importance of several simplified processes, including elastic stress transfer (Ward, 2000; Ben-Zion et al., 2003; Rundle et al., 2004; Richards-Dinger and Dieterich, 2007; Dieterich and Richards-Dinger, 2010), dynamic weakening (Shaw and Rice, 2000; Lapusta et al., 2000), rate-and-state friction (Lapusta et al., 2000; Richards-Dinger and Dieterich, 2007; Dieterich and Richards-Dinger, 2010), and viscoelasticity (Pollitz, 2009). Such simulations have been run on fault networks designed for California (e.g. the San Andreas fault and other major faults), incorporating input parameters such as elastic parameters, rate-and-state friction parameters, and values of static and dynamic failure stress thresholds. They typically result in synthetic seismicity catalogs spanning tens of thousands of years and thousands of $M \gtrsim 6$ events, affording the opportunity to analyze the resulting statistics. Such simulations are presently being explored by the Fault Simulators Group of the Southern California Earthquake Center (SCEC) in order to guide long-term forecasting efforts related to the Unified California Earthquake Rupture Forecast (UCERF). Because of the complexity of physics-based models, it is challenging to compare the results of the simulations. They may share the same fault geometry and incorporation of elastic stress transfer, but available simulator codes diverge

in further capabilities. More fundamentally, sensitivity studies of simulator results with respect to input parameters have been limited. Systematic studies of the dependence of seismicity statistics on input parameters have focussed on strength heterogeneity (Ben-Zion and Rice, 1995; Ben-Zion, 1996; Dieterich and Richards-Dinger, 2010; Yikilmaz, 2010), proxy dynamic overshoot and/or dynamic weakening parameters (Fisher et al., 1997; Dahmen et al., 1998; Ben-Zion et al., 2003; Rundle et al., 2004; Pollitz, 2009), and fault steps (Ward, 2000; Yikilmaz, 2010). These studies have focussed on a number of important questions, including the identification of distinct of regimes of behavior, the identification of phase transitions, and the efficiency of fault interactions. These and related studies make it clear that for applications to long-term earthquake forecasting, it is important to characterize the epistemic uncertainty associated with a synthetic seismicity catalog.

In this study I employ the viscoelastic earthquake simulator of Pollitz (2009). It accounts for the effects of static elastic and time-dependent viscoelastic stress transfer among model faults, layered elasticity and viscoelasticity, and static and dynamic failure stress thresholds. I investigate the epistemic uncertainty associated with the resulting seismicity catalogs, including coefficient of variation (COV), mean recurrence interval, and magnitude-frequency statistics. I find that there is substantial sensitivity to the considered variable parameters, which are mantle viscosity (which affects time-dependent stress transfer) and a slip weakening parameter (which controls how easily a small event can cascade into a larger event).

2 Viscoelastic earthquake simulator

2.1 Generation of synthetic slip events

The viscoelastic earthquake simulator is explained in Pollitz (2009), and we describe it (with modifications) briefly here. Model faults are assumed to reside in an elastic crust which overlies a viscoelastic crust and mantle with a Maxwell viscoelastic rheology. Following Pollitz (2009), the evolving physical variable is the Coulomb failure function, which is a linear combination of the shear stress and normal stress resolved upon an a-priori slip direction along the considered fault surface (Simpson and Reasenberg, 1994). Following Ben-Zion et al. (2003), a static stress threshold (Figure 1) determines the initiation of a slip event. During an event stress on a failing patch drops to the arrest stress level $\sigma_{\rm a}$ and stress is transferred from slipped patches to neighboring patches, which may fail first at the static stress threshold $\sigma_{\rm s}$ and subsequently (during the same event) at the dynamic stress threshold $\sigma_{\rm d}$. The event terminates when no patches exceed either $\sigma_{\rm s}$ or $\sigma_{\rm d}$ as appropriate. It is useful to define a dynamic overshoot coefficient $D = (\sigma_{\rm s} - \sigma_{\rm a})/(\sigma_{\rm s} - \sigma_{\rm d})$, which characterizes how far the stress is reduced in each sub-event below the dynamic stress threshold; I also define the stress reduction parameter $\Delta\sigma = \sigma_{\rm s} - \sigma_{\rm a}$, which is in general larger than the stress drop of the slip event (Pollitz, 2009). Pollitz (2009) used this simple prescription with constant $\Delta\sigma$ (Figure 2) to determine the initiation, propagation, and termination of earthquake ruptures. Here I modify this model to use slip-dependent $\Delta\sigma$ (Figure 2). Below a certain slip value reached on a given patch during an event, here assumed to be 0.7 m, $\Delta\sigma$ has a constant value which is taken

as 10 MPa. At higher slip, $\Delta\sigma$ will increase linearly with slip with slope γ until it reaches the slip value at which $\Delta\sigma$ attains some maximum value, here assumed to be 30 MPa. The choices of minimum slip value (0.7 m) and the maximum stress value are guided by the suggestion of a change in magnitude-area scaling at area $\sim$ 537 km (Hanks and Bakun, 2008) and experimentation with trial $\Delta\sigma$ values to yield magnitude-area statistics similar to Figure 1 of Hanks and Bakun (2008) at larger magnitude. The slip-dependent stress reduction parameter $\Delta\sigma$ is defined separately for each fault patch, so that different patches slipping during the same event may be subject to different stress reduction parameters. As will be explored later, the slip weakening parameter γ has an important effect on resulting seismicity patterns.

During the period between slip events, crustal stress evolves according to the background tectonic loading and through postseismic relaxation – viscoelastic relaxation of the lower crust and mantle in response to the static stress changes imparted from past slip events. The viscoelastic component is calculated on the viscoelastic structure shown in Figure 4 of Pollitz (2009). The lower crust and mantle viscosities are η_c and η_m, and they control how rapidly stress is re-distributed to other faults following a slip event. The 'loading' component for a given fault is constrained in such a way that the sum of the loading component and the static and postseismic stresses are zero when evaluated over an earthquake cycle with an assumed mean recurrence interval. With this constraint, the tectonic loading component amounts to the imposition of backslip on the considered fault at its long-term slip rate evaluated on the completely relaxed viscoelastic model. It is given

by eqn 7 of Pollitz (2009); which represents the net loading rate obtained by summing over all faults. On a fault segment that has a component of long-term aseismic slip, fault creep is implemented by reducing the amount of backslip that the creeping segment contributes to the background tectonic loading (Pollitz and Schwartz, 2008).

2.2 Computational details

If the network has tens of thousands of fault patches, it is for all practical purposes impossible to store all of the possible patch-to-patch interactions in computer memory. This is the primary justification for the Green's function approach described in section 3.1 of Pollitz (2009). The simulator uses quasi-static Green's functions computed a-priori for a large set of source depths, source-to-'receiver' distance and azimuth, and observation depth, the geometry of the dislocation (i.e., dip of the source patch and the rake of slip), as well as the elapsed time since the slip event on the fault patch (section 3.1 of Pollitz (2009)). They embody coseismic and postseismic deformation from prescribed dislocation sources and are calculated using the methods of Pollitz (1996) and Pollitz (1997). The Green's functions are calculated for source patches of dimension 1 km $\times$ 1 km / $\sin(\delta)$, where δ is the dip of the source patch, which corresponds to a discrete set of lower and upper patch depths which are sampled in increments of 1 km. Green's functions are densely sampled in the near-source region in order to capture short-wavelength elastic interactions and less densely with increasing distance from the source. The quasi-static response at distances or azimuths not directly sampled by the a-priori calculated Green's functions are obtained by isotropic spatial in-

terpolation; and similarly in the temporal domain, i.e. for the deformation at times not directly sampled by the a-priori computed Green's functions. All deformation is evaluated at the center of the patches which comprise the fault network.

Computational efficiency is important when considering a relatively large fault network. It is gained in two principal ways. First, a fast multipole method (FMM) (Tullis et al., 2000) in the spatial domain is employed to increase the speed at which elastic interactions are evaluated. For a given heterogeneous slip distribution associated with a relatively large slip event, this involves re-grouping of source patches (i.e. the fault patch centers) to more efficiently calculate the deformation from groups of source patches distant from a given receiver patch. Receiver patches are also re-grouped by employing a mean field approximation, which is again appropriate for groups of receiver patches that are distant from the considered source patches. Second, a temporal FMM is used to combine groups of patches that share a similar dislocation geometry and time of last slip event, as described in section 3.3 of Pollitz (2009).

The complete expression for the time-dependent stress resulting from a history of past slip events is given by eqn 13 of Pollitz (2009). This expression is used to step forward from the current time t to a new time $t + \Delta t$, where Δt is a time increment typically shorter than 0.1 year in this study. At any current time t, the time to the next slip event is estimated based on the current stress state, the proximity of the fault patches to their respective static stress thresholds, and the net loading rate (combination of background loading rate and postseismic relaxation from past slip events).

The time increment Δt is then chosen such that $t + \Delta t$ will slightly exceed the estimated time to the next slip event. A new slip event is initiated and propagated until it terminates as described in section 2.1. Although most slip events are confined to the same contiguous fault, occasionally a slip event will involve more than one fault segment that may even be spatially isolated from other slipped patches.

2.3 Influence of viscoelastic relaxation

To demonstrate the importance of viscoelasticity in time-dependent crustal deformation, I evaluate time-dependent shear strain resulting from a strike-slip event on a 200-km-long fault rupturing the entire extent of a 12-km-thick elastic upper layer. The viscosity of the underlying half-space is 10^{19} Pa s. The elastic parameters are homogeneous and prescribed by bulk modulus $\kappa = 50$ GPa and shear modulus $\mu = 30$ GPa. Figure 5 shows the initial coseismic and subsequent postseismic fault-parallel strain at the surface for 100 years following a synthetic slip event with 5 m slip. In the near-fault region, the postseismic strains act in the sense to reload the fault and hence erode the initial 'stress shadow' (Harris and Simpson, 1996) imparted by the slip event. At distances greater than about two elastic plate thicknesses (i.e. 24 km) from the fault, however, the initial postseismic strains act to further reduce the shear strain, i.e. deepen the shadow, a tendency which is reversed only after about 50 years as the postseismic relaxation becomes longer wavelength and gradually tends to reload the fault at progressively all distances from the fault. This suggests that the details of fault-to-fault stress transfer depend fundamentally on viscoelastic parameters such as elastic

plate thickness and viscosity as well as inter-fault distance, a consideration that is important in an area such as the San Francisco Bay area which has numerous fault strands separated by distances on the order of one to two elastic plate thicknesses (e.g. Pollitz and Schwartz, 2008).

3 Application to California-wide fault network

The fault network used in this study is shown in Figures 3 and 4. It was constructed from an initial fault network − ALLCAL1 −, provided by Steve Ward to the SCEC Fault Simulators Group in June, 2009, that consists of 8000 slip patches, each of dimension ~ 12 km. That network contains both vertical and dipping faults accommodating a combination of strike slip and dip slip events. I have re-discretized this fault network into 100208 patches of dimension 1 km $\times$ 1 km / $\sin(\delta)$, where δ is the dip of the closest patch in the original fault network. These patches share a common set of lower and upper edge depths at intervals of 1 km, i.e., at 0, 1, 2 km depth and so forth down to a maximum source depth of 16 km. Long-term fault slip rates, also supplied by Steve Ward, vary from as little as 0.5 mm/yr on slowly-slipping faults of eastern California to 35 mm/yr on the San Andreas fault (SAF). Finally, aseismicity factors are assigned to portions of the SAF, Hayward, and Calaveras faults in order to account for fault creep.

Input parameters include the specification of the fault network geometry and long-term slip rates as well as simulator parameters: lower crust and mantle viscosities η_c and η_m, dynamic overshoot parameter D, and slip weakening parameter γ. For a given set of input parameters, a simulation is

run for 30000 years starting from an initial stress state. This is prescribed by the stress state resulting from the analytical forward models obtained by Pollitz and Schwartz (2008), described in section 7.2 of Pollitz (2009). Experiments with alternative random initial stress states show that the resulting statistics are practically independent of the initial stress state.

In the simulations I will generally vary mantle viscosity η_m and slip weakening parameter γ while keeping other model parameters fixed I thus choose values $D = 1.25$ and $\eta_c = 4.0 \times 10^{19}$ Pa s which are kept constant in all simulations. The considered variation in mantle viscosity is consistent with the range estimated in geodetic studies of postseismic relaxation (e.g. Thatcher and Pollitz, 2008). In the resulting seismicity catalogs, an 'event' is assigned to a given fault, fault segment, or point on a fault if either (1) at least 50% of the given fault (or fault segment or point) participates in the rupture or (2) at least 50% of the rupture takes place on the given fault (or fault segment or point). This definition embraces behavior ranging from a small rupture of an isolated group of fault patches to multi-segment ruptures and/or relatively long ruptures that similarly involve a selected group of fault patches.

4 Results

4.1 Magnitude-area statistics

Figure 6 shows the magnitude-area statistics on the northern SAF for a simulation with $\eta_m = 1.2 \times 10^{19}$ Pa s and two values of γ. That with $\gamma = 0$ in the left-hand plot represents the case with no slip weakening; that with $\gamma = 2$

MPa/m on the right-hand plot represents a case with slip weakening at fault slip greater than 0.7 m. It is clear that the prescribed slip weakening has a substantial effect on the statistics. Comparison with observed magnitude-frequency statistics (Hanks and Bakun, 2008) indicates that the synthetic statistics with $\gamma = 0$ are deficient in magnitude (or, equivalently, slip) at large areas, while the statistics with $\gamma = 2$ MPa/m roughly match the observed magnitude-area observations for area $\gtrsim 40$ km^2.

The magnitude-area relationship for $\gamma = 0$ in Figure 6 is consistent with three principal regimes of faulting, though they are not independently constrained by the magnitude-area statistics because of the scatter. The first is the 'fractal slip' regime characterized by groups of patches that are incoherently interconnected and slip almost independently of one another, yielding seismic potency P roughly proportional to area A (Ben-Zion, 2008). This regime exists because of the discrete minimum patch size being employed (1 km^2), and slip is approximately constant (slip $\sim A^0$). This regime is empirically found operable up to ruptures of area roughly twenty times the smallest patch size, i.e. up to about M5.6 - 5.7, beyond which the slipping patches become more organized and interconnected. The second corresponds to a crack expanding in an infinite elastic solid under a uniform stress field, which yields $P \sim A^{3/2}$ (Eshelby, 1957; Knopoff, 1958) and slip proportional to $\sqrt{A}$. This regime operates up to about M7.1, beyond which the rupture is bounded in the vertical dimension (i.e., the fault width cannot exceed the width of the seismogenic zone). The third regime corresponds to a crack expanding in an elastic solid bounded in one dimension, for which slip approaches an asymptotic limit which may be related to the width of the seismogenic zone

and the stress drop (Knopoff, 1958; Maruyama, 1966), so that $P \sim A$ (slip again $\sim A^0$). The observed magnitude-area relationship suggests that at $M \gtrsim 7.2$, $P \sim A^x$, where x may be between 1 and 4/3 (Hanks and Bakun, 2008). The use of $\gamma = 2$ MPa/m allows slip to grow faster than A^0 and thus better replicate the observed magnitude-area relationship.

4.2 Magnitude-frequency statistics

Figure 7 shows magnitude-frequency statistics from a simulation with slip weakening ($\gamma = 2$ MPa/m) on ten selected faults. These statistics generally exhibit three domains. At magnitudes less than 5.6 the slipping patches are not well connected and occur less frequently than events which cascade coherently into larger events. At magnitudes ranging from 5.6 to about $6.3-7.0$ (depending on fault length), the statistics obey a Gutenberg-Richter relationship with a $b-$value ranging from 0.9 to 1.7. At larger magnitude the statistics are roughly Gaussian about a mean magnitude $\bar{M}$ characteristic of the largest events that can occur on that fault. This behavior conforms to the combined Gutenberg-Richter and characteristic earthquake model of Wesnousky (1994) deduced from joint seismic and paleoseismic data. It is represented schematically in Figure 4.1 of Working Group on California Earthquake Probabilities (2003). Repeating eqn 22 of Pollitz (2009), I quantify this behavior with a non-characteristic probability density function

(pdf) with slope $-b$ and a characteristic pdf:

$$\log_{10} f = \begin{cases} \log_{10}\left\{\frac{\dot{N}(M^0)\beta\exp\left[-\beta(M-M^0)\right]}{1-\exp[-\beta(M^{\mathrm{u}}-M^0)]}\right\} & M < \bar{M} - 2\sigma_M \\ \\ \log_{10}\left\{c\exp\left\{-\frac{1}{2}\left[\frac{(M-\bar{M})}{\sigma_M}\right]^2\right\}\right\} & M \geq \bar{M} - 2\sigma_M \end{cases} \quad (1)$$

where $\beta = b\ln 10$ and c is a constant associated with the distribution of events of characteristic magnitude $\bar{M}$ with Gaussian half-width σ_M. Following Youngs and Coppersmith (1985) the non-characteristic pdf is a truncated Gutenberg-Richter distribution with minimum magnitude M^0, maximum magnitude M^{u}, and rate of earthquake production at magnitude above M^0 equal to $\dot{N}(M^0)$. I choose $M^{\mathrm{u}} = \bar{M} - 2\sigma_M$ and $M^0 = 5.0$. An observed magnitude-frequency distribution may be optimally fit for all constants by performing a grid search over $\bar{M}$ and σ_M and, for each set of trial values, solving for $\dot{N}(M^0), b, c$ in a least squares inversion. The information for $M < 5.6$ is excluded in these inversions. The values of optimal b and $\bar{M}$ are summarized for each magnitude-frequency distribution in Figure 7. Figure 8 shows the corresponding cumulative probability and its fit with eqn 1.

A clear characteristic earthquake peak is discerned for all of the strike-slip faults in Figure 7. The dominant controlling factor in the value of $\bar{M}$ is the fault length, longer faults tending to have larger $\bar{M}$. An exception is the northern Calaveras fault, which has $\bar{M} = 7.26$, although the largest realized event with M=7.45 is much smaller than the largest realized event on the southern SAF (M=7.75) or the northern SAF (M=7.85). Time-dependent fault interaction appears to play a role in the long-term statistics,

since b and $\bar{M}$ for the smallest faults adjacent to a major fault, i.e. the Hayward, Rodgers Creek, and northern Calaveras faults, are sensitive to mantle viscosity, as will be explored in the next section.

4.3 Mean inter-event times

Figure 9 presents histograms of inter-event times on the same ten faults considered in Figure 7. The magnitude threshold for each fault is chosen close to the characteristic magnitude on that fault. The inter-event time distributions exhibit a wide variety of behavior, from peaked about a single mean recurrence interval (Hayward fault), to double-peaked (Rodgers Creek and Macaama faults) to widely scattered (northern Calaveras fault). Similar behavior is seen in other large-scale simulations, e.g. Figure 5 of Dieterich and Richards-Dinger (2010), though specific behavior generally depends in a complicated fashion on controlling parameters of the simulation. The bimodal distribution for the Rodgers Creek fault in Figure 9 is remarkable, with two peaks of order 250 and 700 years, respectively. These are close to the combined mean recurrence intervals of the Hayward and Maacama faults. (The Maacama fault has roughly the same double peak in inter-event times, and the Hayward fault is peaked at the shorter inter-event time.) This suggests that the timing of larger-magnitude, characteristic events is to a large extent controlled by the recurrence times of the largest events sustainable on the faults which approach the endpoints of the Rodgers Creek fault from its southern and northern ends.

5 Epistemic uncertainty in seismicity statistics

I explore the sensitivity of simulation results to controlling parameters, particularly mantle viscosity η_m. This affords us an opportunity to understand the influence of a single physical parameter on the statistics and hence the epistemic uncertainty, as well as gain insight into the behavior of the fault system as a whole.

Referring to Figure 10, Figure 11 shows the history of slip along the northern SAF for a 10000-year time interval (beginning 12000 years into the simulation) for a simulation with $\eta_m = 1.2 \times 10^{19}$ Pa s and $\gamma = 2$ MPa/m. This rich history of slip illustrates the importance of segment boundaries. At the Golden Gate, Pt. Arena, and Shelter Cove, the SAF has either a marked change in strike, a slight lateral step, or a change in slip rate. The Golden Gate marks a change in strike as well as slip rate, which is 17 mm/yr to its south and 24 mm/yr to its north; the change in slip rate is achieved with a gradual increase from south to north over a 20-km distance along the SAF. These segment boundaries are long-lived partial barriers to slip. The slip budget on relatively short fault sub-segments must often be filled in with moderate (M = 6.5 to 7.0) events because of the relatively low slip of the larger events in the vicinity of the segment boundaries. A segment 'boundary' itself appears to migrate over periods of thousands of years as successive large-slip events propagate to the slip endpoints remaining from past slip events, approaching from both the south and north. Only at Shelter Cove, where there is a large change in strike, does the boundary remain essentially fixed. Note that the presence of these boundaries prevents the

occurrence of a single through-going event along the entire northern SAF. Similar effects of segmentation on seismicity patterns in northern California are seen in Figure 10 of Ward (2000).

Similar patterns are seen in the corresponding history of slip on the southern SAF (Figure 12). The most pronounced slip barriers are at the San Bernardino - Mojave segment boundary and Carrizo Plain - Cholame segment boundary. In the former case this is associated with a transition in slip rate, the San Bernardino and Mojave segments having average slip rates of 24 mm/yr and 30 mm/yr, respectively. The slip rates are identical on the Cholame and Carrizo Plain segments, but there is a ~ 0.5 km step in the fault network at their common boundary (which is not implied to be realistic) which makes it a partial barrier to slip propagation in large events. Figure 13 shows the corresponding slip history for the case $\eta_m = 3 \times 10^{19}$ Pa s. A key difference from the pattern obtained with $\eta_m = 1.2 \times 10^{19}$ Pa s is an enhancement of slip barriers at segment boundaries. For example, the San Bernardino - Mojave segment boundary permits fewer large slip events to cross it in the high-viscosity case (Figure 13) compared with the low-viscosity case (Figure 12), and the slip budget near the boundary must be completed with more moderate events. This suggests that mantle viscosity may control fundamentally different slip regimes, as has been investigated for other parameters by Fisher et al. (1997) and Dahmen et al. (1998).

Although Figure 6 indicates several ruptures longer than 250 km on both the northern and southern SAF during the 30000-year catalog, events of magnitude ≥ 7.7 occur on the SAF only every few thousands of years, far less often than thought to actually occur (e.g. Biasi et al., 2002; Fumal

et al., 2002b,a). Moreover, other earthquake simulators (e.g. Virtual California (Rundle et al., 2004) or that of Ward (2000)) running on the original ALLCAL1 network yield $M \geq 7.7$ ruptures on the SAF every few hundreds of years. It is clear that the segment boundaries implemented in the present study are effective at inhibiting rupture. Both slip rate discontinuities and fault steps at segment boundaries are at the root of this. The original ALLCAL1 fault model consists of fault patches of dimension ~ 3 km. A chief difference between the present simulations and those of related simulators is the use of a relatively small fault patch size (1 km) in the present study (realized by re-discretizing ALLCAL1). Even a modest fault step of 0.5 km, as exists at the Cholame-Carrizo Plain segment boundary, is a large fraction of the fault patch size, and slip cannot easily extend through such a fault step. I suggest that both the existence of such fault steps as well as the present approach for mimicking slip weakening (through the parameter γ) may make segment boundaries less penetrable than they ought to be. Use of a fault network designed for a relatively small patch size may improve this in future simulations.

Figures 14 and 15 show $b-$value and characteristic magnitude $\bar{M}$ as a function of η_m derived from inter-event time distributions on selected faults. It is noteworthy that (with the exception of $b-$value for the Concord / Green valley fault) both measures are robust, with only modest variation as a function of η_m, though a systematic trend with η_m may exist as discussed below.

Figures 16 and 17 show COV and mean recurrence interval T as a function of η_m on selected faults at two magnitude thresholds: $M > 6.7$ for

three shorter faults and $M > 7.3$ for three segments that are part of much longer faults. The uncertainty in T is obtained by simple means of sampling ten independent, non-overlapping sub-catalogs of the complete seismicity catalog, calculating T in each sub-catalog and the corresponding variance; this uncertainty is generally much smaller than the spread in T as measured by COV. It is noteworthy that while T is robust with respect to variations in viscosity, COV shows considerable scatter. The scatter in COV is most pronounced for the fault segments belonging to the larger faults, particularly the considered point on the northern San Jacinto fault. This may be because this point is located just south of the junction of the northern San Jacinto fault with the SAF San Bernardino segment, where it is especially susceptible to episodic stress perturbations from large events on the SAF. For $\eta_m = 0.75 \times 10^{19}$ Pa s, COV for the northern San Jacinto fault is 0.63 (Figure 16). COV for the San Jacinto/Anza segment as a whole at the same magnitude threshold ($M > 7.3$) is smaller (0.51), supporting the interpretation that interaction with a neighboring fault (e.g. SAF) has a major influence on point estimates of COV.

Systematic trends in the statistics with respect to mantle viscosity may exist for M and T. Figures 15 and 17 suggest that M tends to decrease and T tends to decrease with increasing η_m. This may be quantified with linear fits of the form

$$\begin{aligned} M(\eta_m) &= A_M + B_M \log_{10} \frac{\eta_m}{\eta_0} \\ T(\eta_m) &= A_T + B_T \log_{10} \frac{\eta_m}{\eta_0} \end{aligned} \tag{2}$$

where η_0 is an arbitrary reference viscosity. Figure 18 shows the estimated values of B_M and B_T. The identified trends are not statistically significant for any one fault but, taken as a whole, are suggestive of systematic behavior. These trends, if real, are consistent with the expectation that M and T be anticorreslated in order to satisfy the slip budget on each fault.

6 Conclusions

In synthetic simulations of seismicity, common statistical measures of seismicity are sensitive to the physical parameters controlling its behavior, including a dynamic overshoot parameter (equivalent to the ratio of dynamic and static strengths), a slip weakening parameter, and mantle viscosity η_m. We have concentrated on the effect of η_m on several such measures (magnitude-frequency statistics, mean recurrence interval, COV). With a set of 30000-year-long synthetic catalogs, it is difficult to ascertain systematic variations in these statistics with variations in viscosity, though the measures M and T – characteristic magnitude and mean recurrence interval, respectively – may exhibit a systematic dependence in viscosity. If real, it would mean that epistemic uncertainty in these measures, i.e. 0.2 - 0.3 magnitude units in M and up to 20% variations in T, may be reduced, in principle, if their dependence on a key physical parameter were better understood. Overall, the obtained variations in statistical seismicity measures are likely related to systematic effects in the complex fault interactions that occur given the presence of time and space-dispersive post-earthquake relaxation following large events. Slip maps for the northern SAF and southern

SAF, each summarizing 10000 years of seismicity, show the lasting effects of segment boundaries on seismicity patterns. A comparison of slip maps for the southern SAF obtained with different mantle viscosity suggests that the 'slip barrier' nature of a segment boundary depends substantially on the mantle viscosity. These and trial simulations with alternative fault networks also suggest that the fine details of fault geometry, including the presence of fault steps, have a major influence on the resulting seismicity patterns.

Data and Resources. No data were used in this paper. Some plots were made using the Generic Mapping Tools version 4.2.1 (www.soest.hawaii.edu/gmt; Wessel and Smith, 1998).

Acknowledgments. I am grateful to Steven Ward for providing the all-California fault network used in this study. I thank two anonymous reviewers and David Chapman for constructive comments which improved this paper.

References

Ben-Zion, Y. (1996). Stress, slip, and earthquakes in models of complex single-fault systems incorporating brittle and creep deformations. *J. Geophys. Res.*, 101:5677–5706.

Ben-Zion, Y. (2008). Collective behavior of earthquakes and faults: Continuum-discrete transitions, evolutionary changes and corresponding dynamic regimes. *Rev. Geophys.*, page doi:10.1029/2008rg000260.

Ben-Zion, Y., Eneva, M., and Liu, Y. (2003). Large earthquake cycles and

intermittent criticality on heterogeneous faults due to evolving stress and seismicity. *J. Geophys. Res.*, 108:2307,doi:10.1029/2002JB002121.

Ben-Zion, Y. and Rice, J. R. (1995). Slip patterns and earthquake populations along different classes of faults in elastic solids. *J. Geophys. Res.*, 100:12959 12983.

Biasi, G., Weldon II, R. J., Fumal, E., and Seitz, G. G. (2002). Paleoseismic event dating and the conditional probability of large earthquakes on the southern san andreas fault, california,. *Bull. Seismol. Soc. Am.*, 92:2761–2781.

Dahmen, K., Ertas, D., and Ben-Zion, Y. (1998). Gutenberg-Richter and characteristic earthquake behavior in simple mean-field models of heterogeneous faults. *Physical Review E*, 58:1494–1501.

Dieterich, J. and Richards-Dinger, K. (2010). Earthquake Recurrence in Simulated Fault Systems. *Pure Appl. Geophys.*, 167:1087–1104.

Eshelby, J. D. (1957). The determination of the elastic field of an ellipsoidal inclusion and related problems. *Proc. R. Soc. London Ser. A*, 241:376–396.

Fisher, D. S., Dahmen, K., Ramanathan, S., and Ben-Zion, Y. (1997). Statistics of earthquakes in simple models of heterogeneous faults. *Phys. Rev. Lett.*, 78:4885–4888.

Fitzenz, D. D. and Miller, S. A. (2004). New insights on stress rotations from a forward regional model of the San Andreas Fault system

near its Big Bend in southern California. *J. Geophys. Res.*, 109:B08404, doi:10.1029/2003JB002890.

Fumal, T. E., Rymer, M. J., and Seitz, G. G. (2002a). Timing of large earthquakes since A.D. 800 on the Mission Creek strand of the San Andreas fault zone at Thousand Palms Oasis, near Palm Springs, California. *Bull. Seismol. Soc. Am.*, 92:2841–2860.

Fumal, T. E., Weldon II, R. J., Biasi, G. P., Dawson, T. E., Seitz, G. G., Frost, W. T., and Schwartz, D. P. (2002b). Evidence for large earthquakes on the San Andreas fault at the Wrightwood, California, paleoseismic site: A.D. 500 to Present. *Bull. Seismol. Soc. Am.*, 92:2726–2760.

Hanks, T. and Bakun, W. H. (2008). M-logA Observations for Recent Large Earthquakes. *Bull. Seismol. Soc. Am.*, 98:490–494.

Harris, R. A. (2004). Numerical simulations of large earthquakes: dynamic rupture propagation on heterogeneous faults. *Pure Appl. Geophys.*, 161:2171–2181.

Harris, R. A. and Simpson, R. W. (1996). In the shadow of 1857- Effect of the Great Ft. Tejon Earthquake on subsequent earthquakes in southern California. *Geophys. Res. Lett.*, 23:229–232.

Knopoff, L. (1958). Energy release in earthquakes. *Geophys. J.*, 1:44–52.

Lapusta, N., Rice, J. R., Ben-Zion, Y., and Zheng, G. (2000). Elastodynamic analysis for slow tectonic loading with spontaneous rupture

episodes on faults with rate- and state-dependent friction. *J. Geophys. Res.*, 105:23765–23789.

Maruyama, T. (1966). On two-dimensional elastic dislocations in an infinite and semi-infinite medium. *Bull. Earthq. Res. Inst.*, 44:811–871.

Pollitz, F. F. (1996). Coseismic deformation from earthquake faulting on a layered spherical earth. *Geophys. J. Int.*, 125:1–14.

Pollitz, F. F. (1997). Gravitational viscoelastic postseismic relaxation on a layered spherical earth. *J. Geophys. Res.*, 102:17921–17941.

Pollitz, F. F. (2009). A viscoelastic earthquake simulator, with application to the San Francisco Bay region. *Bull. Seismol. Soc. Am.*, 99:1760–1785.

Pollitz, F. F. and Schwartz, D. S. (2008). Probabilistic seismic hazard in the San Francisco Bay area based on a simplified viscoelastic-cycle model of fault interactions. *J. Geophys. Res.*, 113:B05409, doi :10.1029/2007JB005227.

Richards-Dinger, K. and Dieterich, J. (2007). Earthquake occurrence in regional-scale fault models with rate- and state-dependent friction. *EOS Trans. AGU*, 88(52):Fall Meet. Suppl., abstract S21C–0719.

Robinson, R. and Benites, R. A. (1995). Synthetic seismicity models of multiple interacting faults. *J. Geophys. Res.*, 100:18229–18238.

Robinson, R. and Benites, R. A. (1996). Synthetic seismicity models for the Wellington Region, New Zealand : implications for the temporal distribution of large events. *J. Geophys. Res.*, 101:27833–27844.

Rundle, J. B., Rundle, P. B., Donnellan, A., and Fox, G. (2004). Gutenberg-Richter statistics in topologically realistic system-level earthquake stress-evolution simulations. *Earth Planets Space*, 56:761–771.

Rundle, J. B., Tiampo, K. F., Klein, W., and Sa Martins, J. S. (2002). Self-organization of leaky threshold systems: the influence of near-mean field dynamics and its implications for earthquakes, neurobiology, and forecasting. *Proc. Natl. Acad. Sci. U.S.A.*, 99 Suppl 1:2514–2521.

Shaw, B. E. and Rice, J. R. (2000). Existence of continuum complexity in the elastodynamics of repeated fault ruptures. *J. Geophys. Res.*, 105:23791–23810.

Simpson, R. W. and Reasenberg, P. A. (1994). Earthquake-induced static stress changes on central California faults. In Simpson, R. W., editor, *The Loma Prieta, California, earthquake of October 17, 1989 – tectonic processes and models*, volume 1550-F, pages 55–89.

Thatcher, W. and Pollitz, F. F. (2008). Temporal evolution of continental lithospheric strength in actively deforming regions. *GSA Today*, 18:4–11.

Tullis, T. E., Salmon, J., and Kato, N. (2000). Use of fast multipoles for earthquake modeling. *Proceedings of Second ACES Workshop, Tokyo and Hakone, Japan, Oct. 15-20*, pages 35–40.

Ward, S. N. (2000). San Francisco bay area earthquake simulations, a step towards a standard physical model. *Bull. Seismol. Soc. Am.*, 90:370–386.

Wesnousky, S. G. (1994). The Gutenberg-Richter or characteristic earthquake distribution, Which is it? *Bull. Seismol. Soc. Am.*, 84:1940–1959.

Working Group on California Earthquake Probabilities (2003). Earthquake probabilities in the San Francisco Bay region. *U.S. Geological Survey Open-file Report*, 03-214.

Yikilmaz, M. B. (2010). *Studies of Fault Interactions and Regional Seismicity Using Numerical Simulations*. PhD thesis, Univ. of California, Davis.

Youngs, R. and Coppersmith, K. (1985). Implications of fault slip rates and earthquake recurrence models to probabilistic seismic hazard estimates. *Bull. Seismol. Soc. Am.*, 75:939–964.

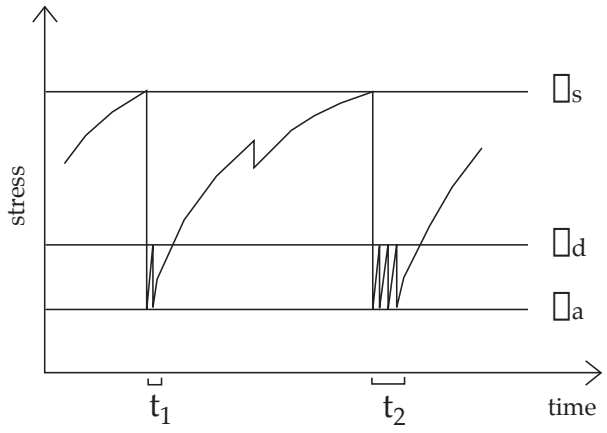

Figure 1: Stress history of a patch that had a slip event at times t_1 and t_2. An event is initiated when stress attains the static frictional stress $\sigma_{\rm s}$. The fault patch slips the amount necessary to reduce its stress to the arrest stress level τ_a in isolation. During an event, if stress on the same patch attains the dynamic friction value $\sigma_{\rm d}$, it will slip again an amount necessary to reduce its stress to $\sigma_{\rm a}$. Immediately after an event, the final stress may be different from $\sigma_{\rm a}$ because of the interaction of neighboring fault patches. The slippage during events at times t_1 and t_2 is not of finite duration (as depicted) but occurs instantaneously in the static cascade model. During the interseismic period the patch stressing rate with depart from linearity because of crust and mantle viscoelastic relaxation, and stress steps between slip events may arise from slip events on neighboring faults. (Figure is repeated from Pollitz (2009).)

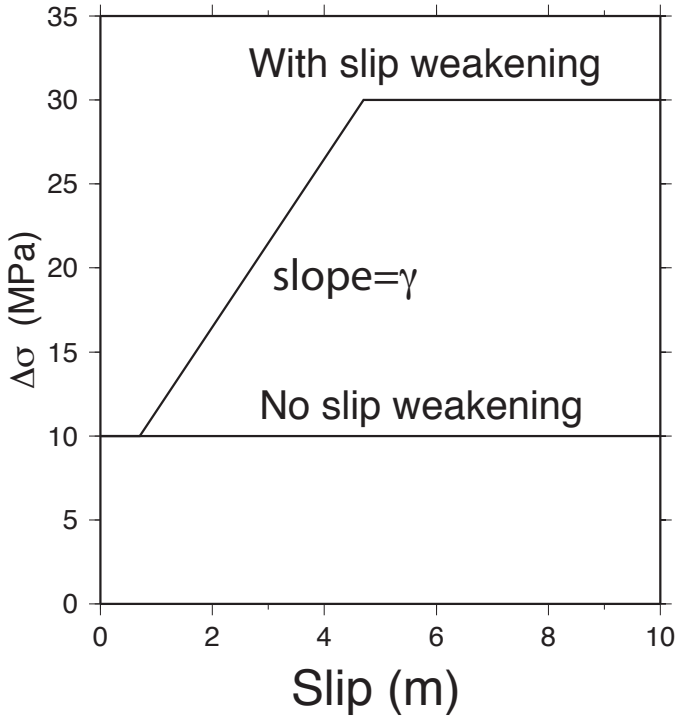

Figure 2: Slip dependence of the stress reduction parameter $\Delta\sigma$. In the case of no slip dependence, $\Delta\sigma$ is constant. In the case of slip-dependent $\Delta\sigma$, $\Delta\sigma$ is constant for slip between zero and 0.7 m, at which $\Delta\sigma = 10$ MPa, and $\Delta\sigma$ increases with slope γ MPa/m until the slip value at which $\Delta\sigma$ attains a value of 30 MPa.

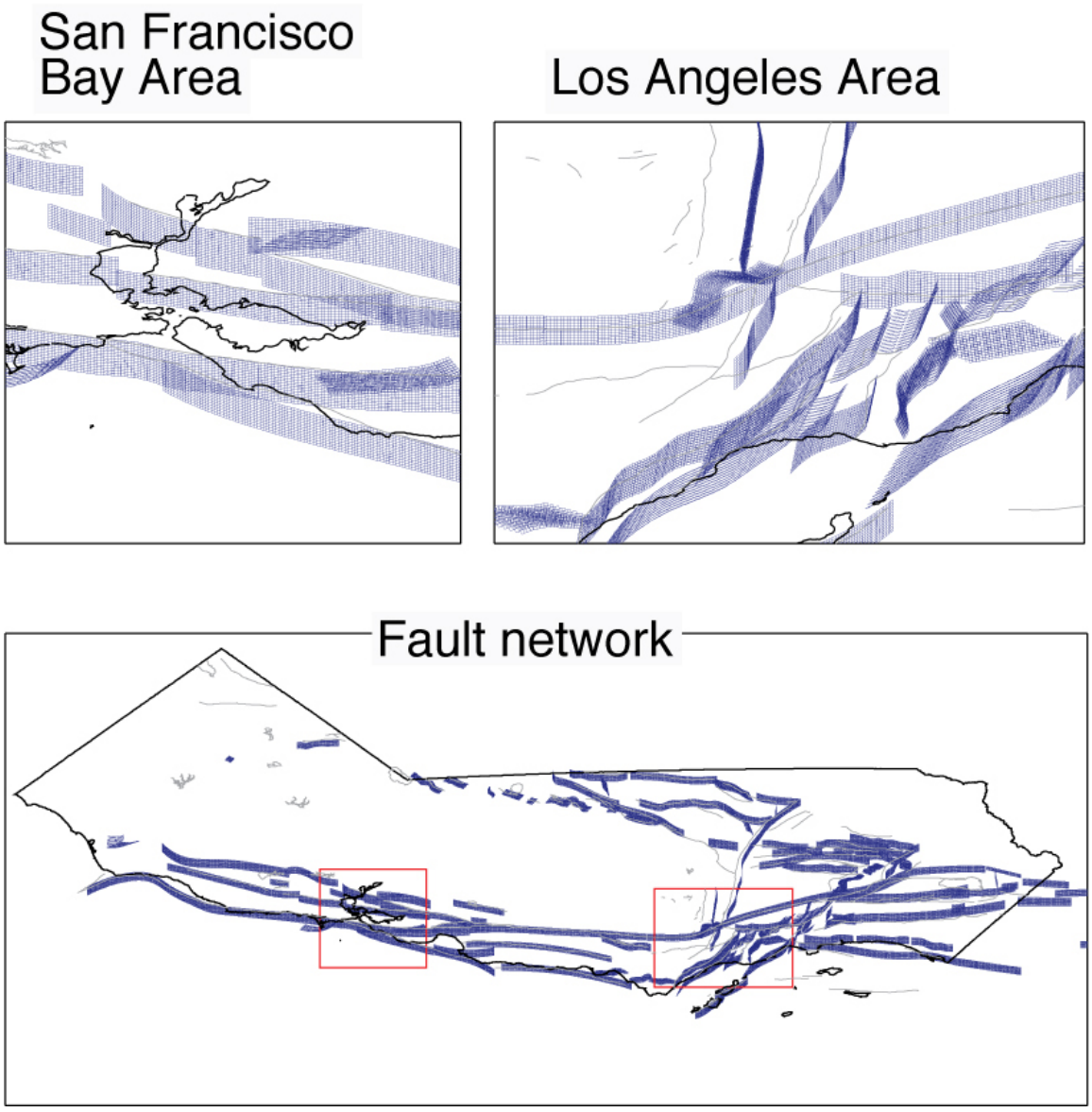

Figure 3: Fault network used in this study, consisting of 100208 patches of dimension 1 km^2 for vertical faults and 1 km^2/$sin(\delta)$ for dipping patches, where δ is fault dip. It is a re-discretized version of an 8000-patch network originally provided by Steve Ward.

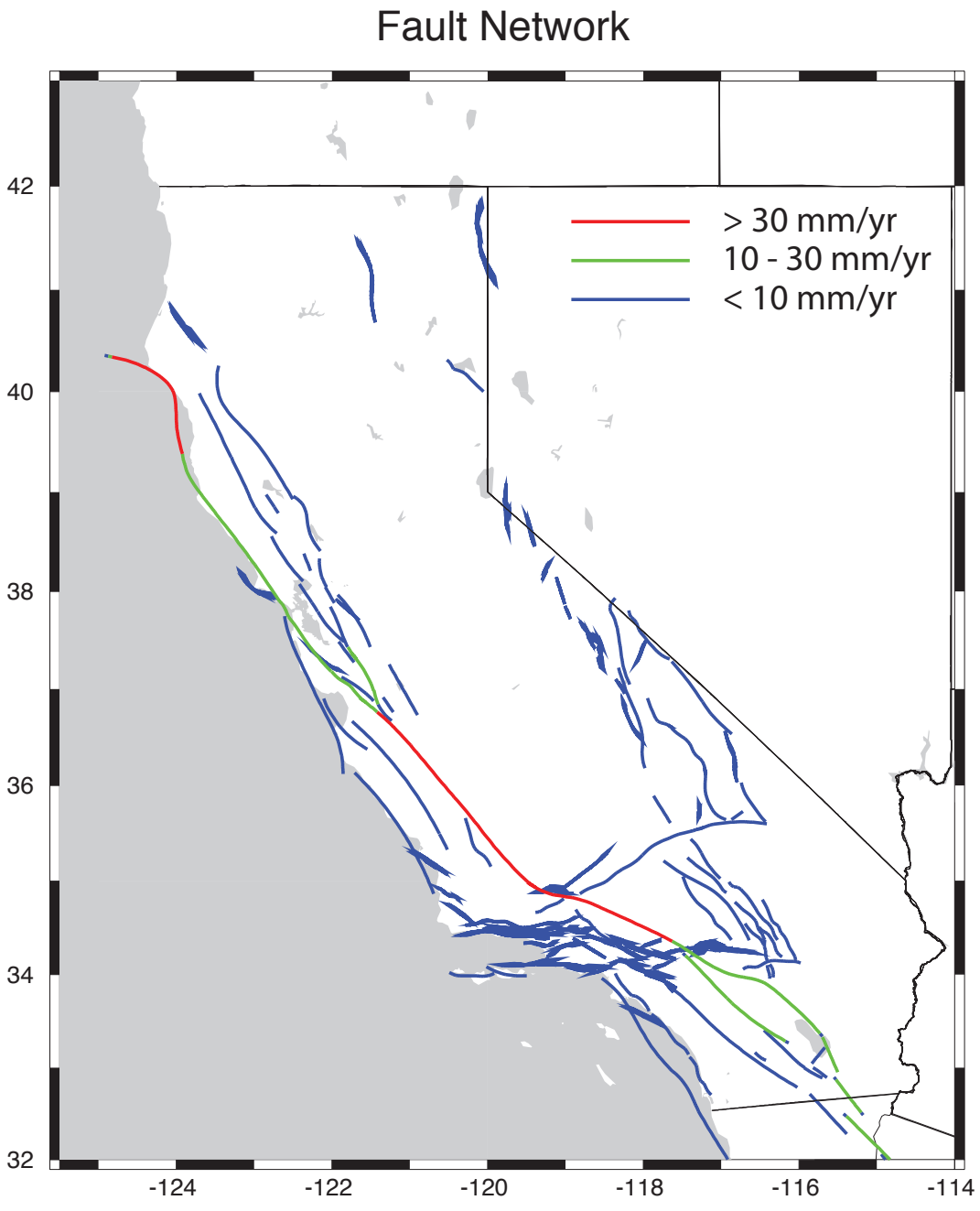

Figure 4: Surface projection of the fault network of Figure 3 shown in map view. Blue, green, and red faults correspond to long-term slip rates < 10 mm/yr, between 10 and 30 mm/yr, and > 30 mm/yr, respectively.

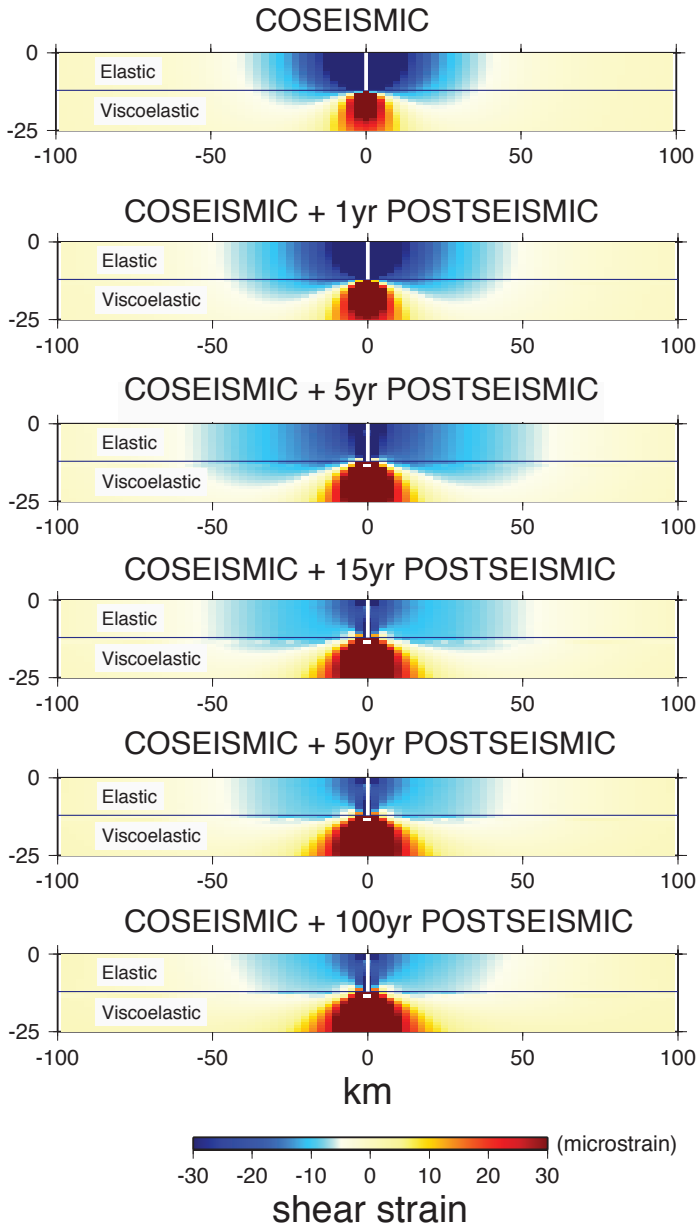

Figure 5: Evolution of fault-parallel shear strain resulting from a strike-slip event (slip = 5 m) on a 200 km long fault rupturing an elastic upper plate of thickness 12 km. The viscosity of the underlying half-space is 10^{19} Pa s. Each depth section is taken on a profile bisecting the fault and perpendicular to it.

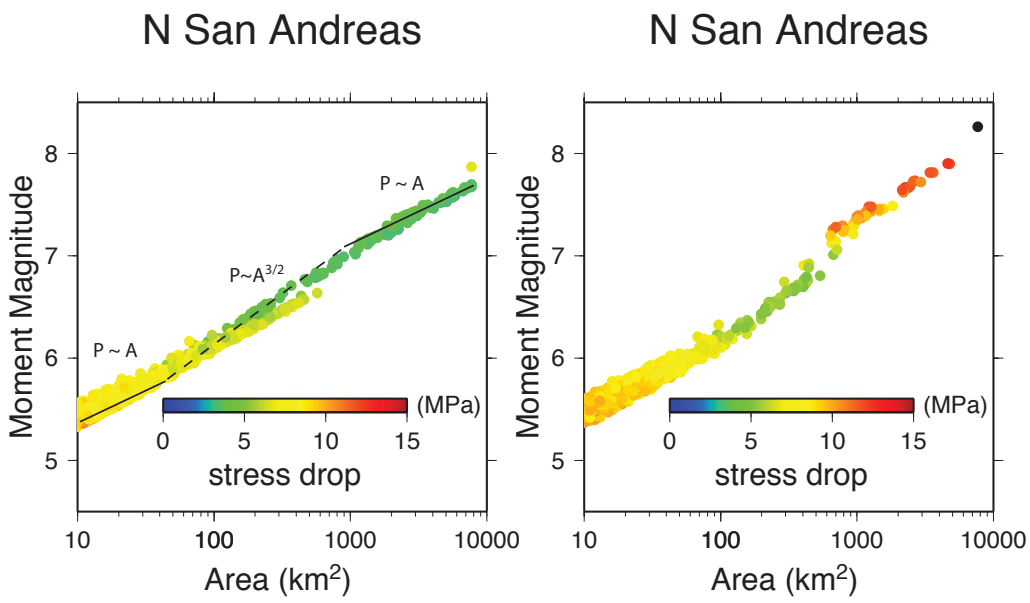

Figure 6: Moment magnitude versus area for events on the northern San Andreas fault for a simulation with $\eta_m = 1.2 \times 10^{19}$ Pa s and $\gamma = 0$ (left) and $\gamma = 2$ MPa/m. Solid and dashed lines indicate regimes of theoretical potency P vs. area A. (right). Color shading indicates the mean stress drop associated with each slip event.

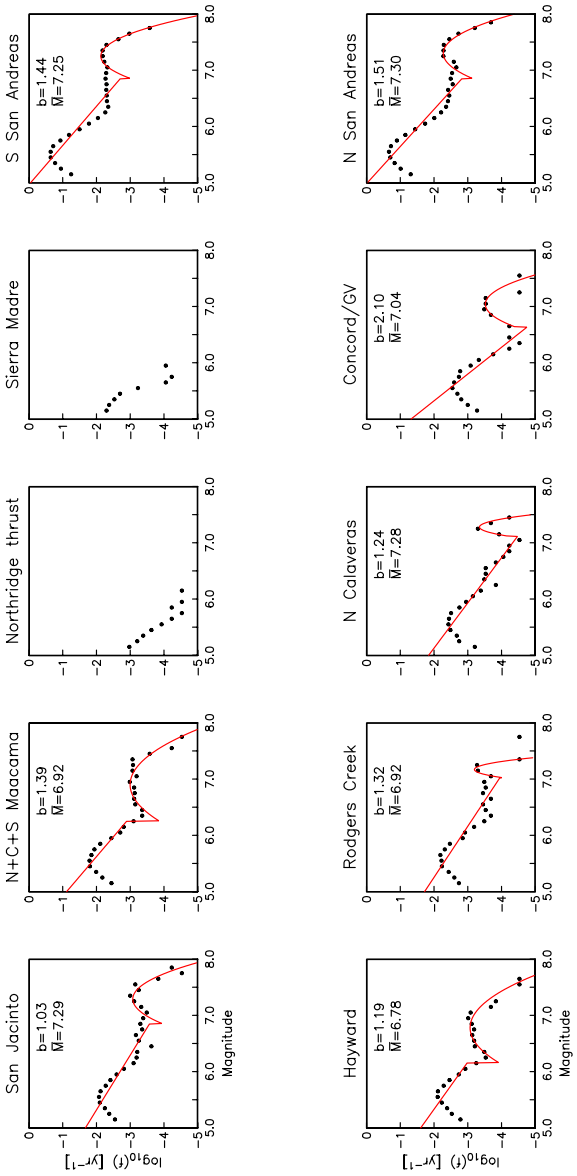

Figure 7: Frequency of earthquake occurrence on selected faults for a simulation with $\eta_m = 1.2 \times 10^{19}$ Pa s and $\gamma = 2$ MPa/m. Event frequency is compiled in bins of 0.1 magnitude unit. Superimposed in red for each distribution is the best-fitting curve given by eqn 1. The synthetic data are not sufficient to determine the parameters for the thrust faults (Northridge thrust; Sierra Madre fault).

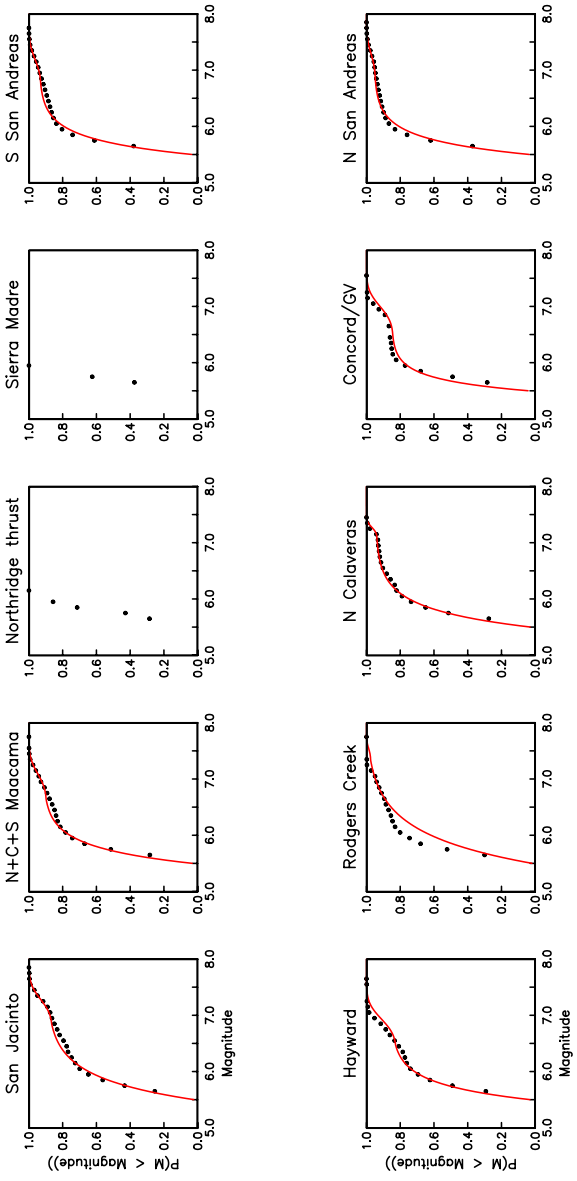

Figure 8: Cumulative probability versus moment magnitude for the marginal frequency distributions shown in Figure 7 at magnitude ≥ 5.6. Superimposed in red for each distribution is the best-fitting curve given by the integral of eqn 1 with respect to magnitude.

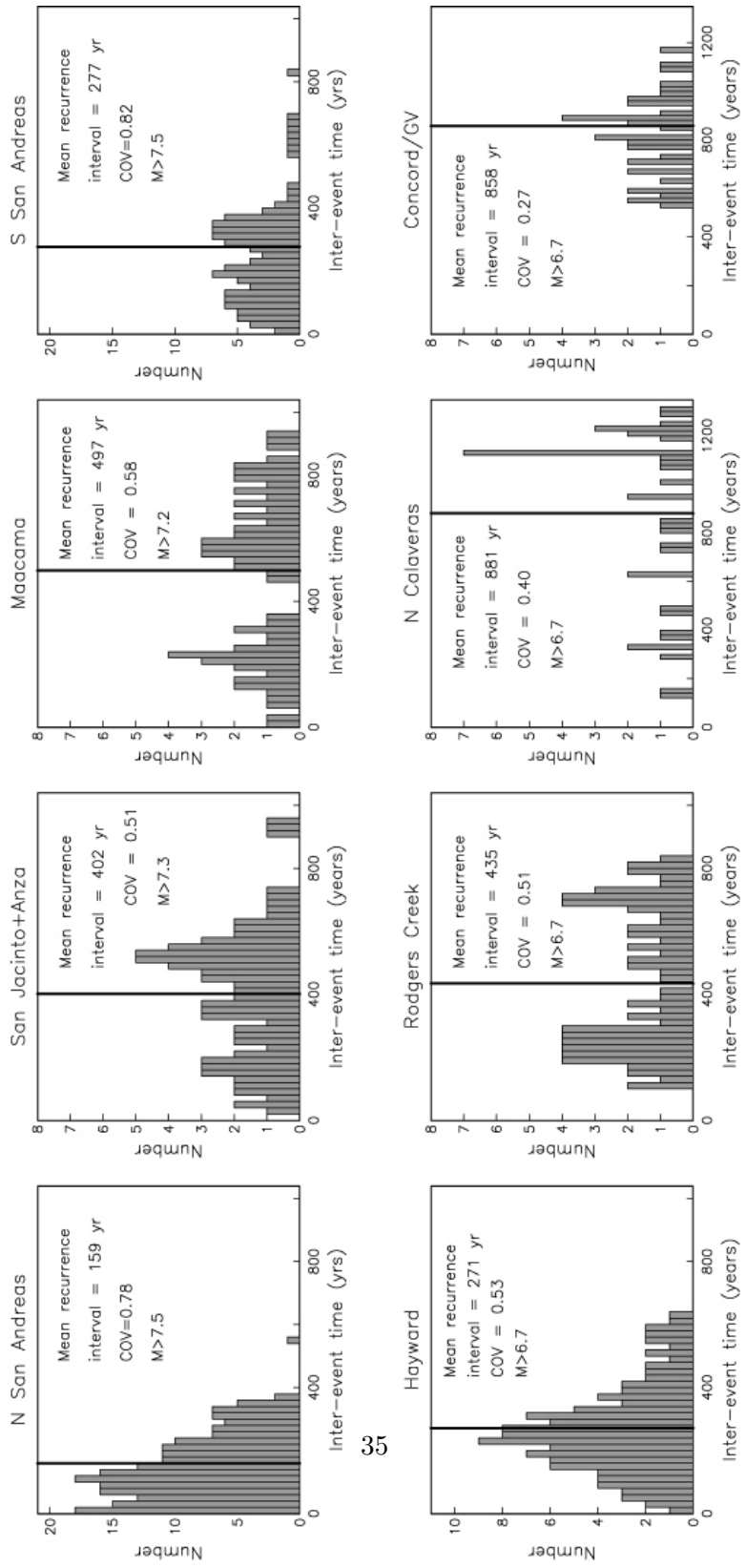

Figure 9: Histograms of inter-event times on selected faults at the indicated magnitude thresholds for a simulation with $\eta_m = 1.2 \times 10^{19}$ Pa s and $\gamma = 2$ MPa/m. Inter-event time is compiled in bins of length 20 years. Black

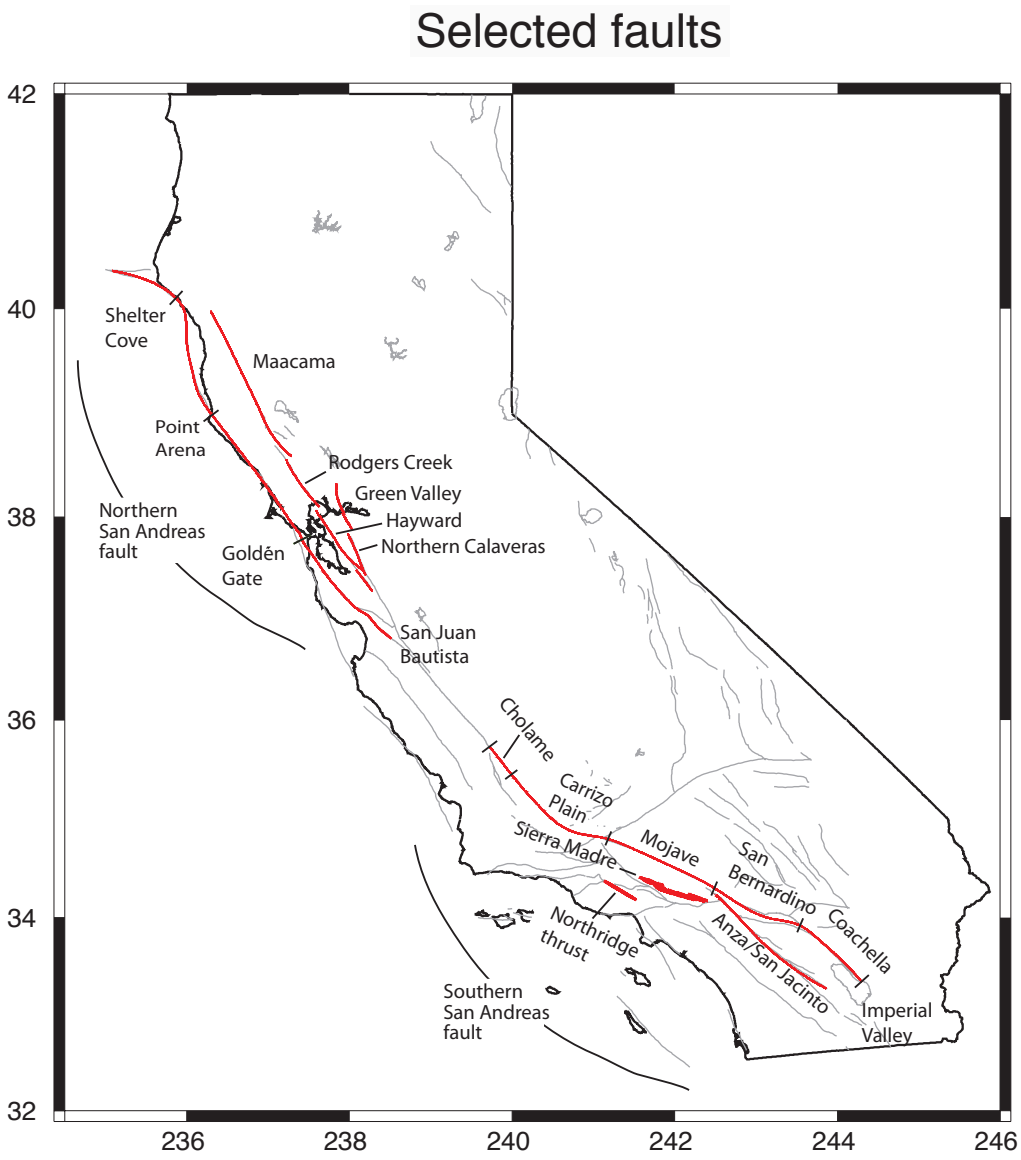

Figure 10: Background map of localities and fault names referred to in Figures 11, 12, and 13. Gray lines indicate traces of active faults.

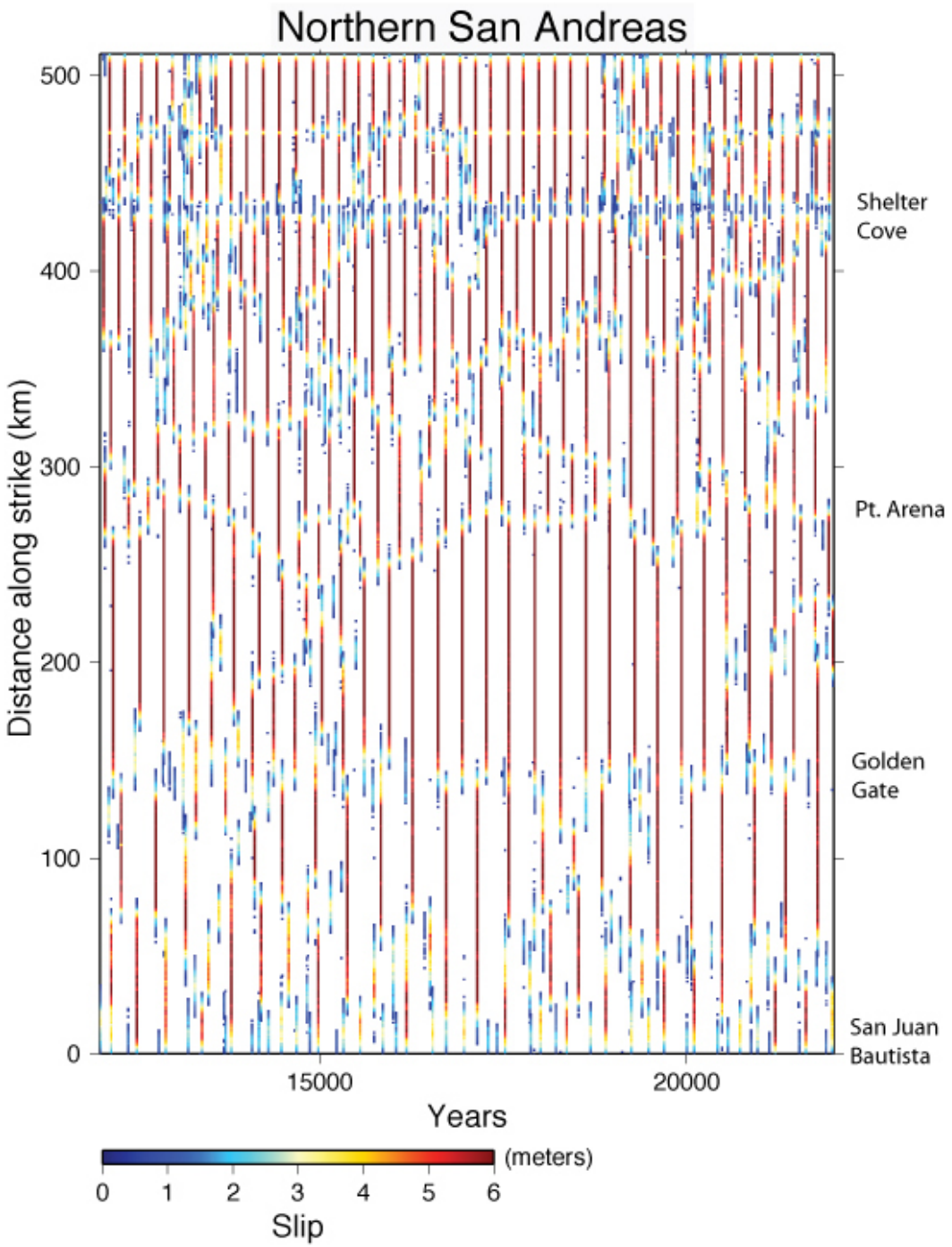

Figure 11: Slip map of the northern San Andreas fault for a 10000-year period, showing slip as a function of time and distance along strike, measured north from San Juan Bausista, for all $M > 6.5$ events. Simulation parameters are $\eta_m = 1.2 \times 10^{19}$ Pa s and $\gamma = 2$ MPa/m.

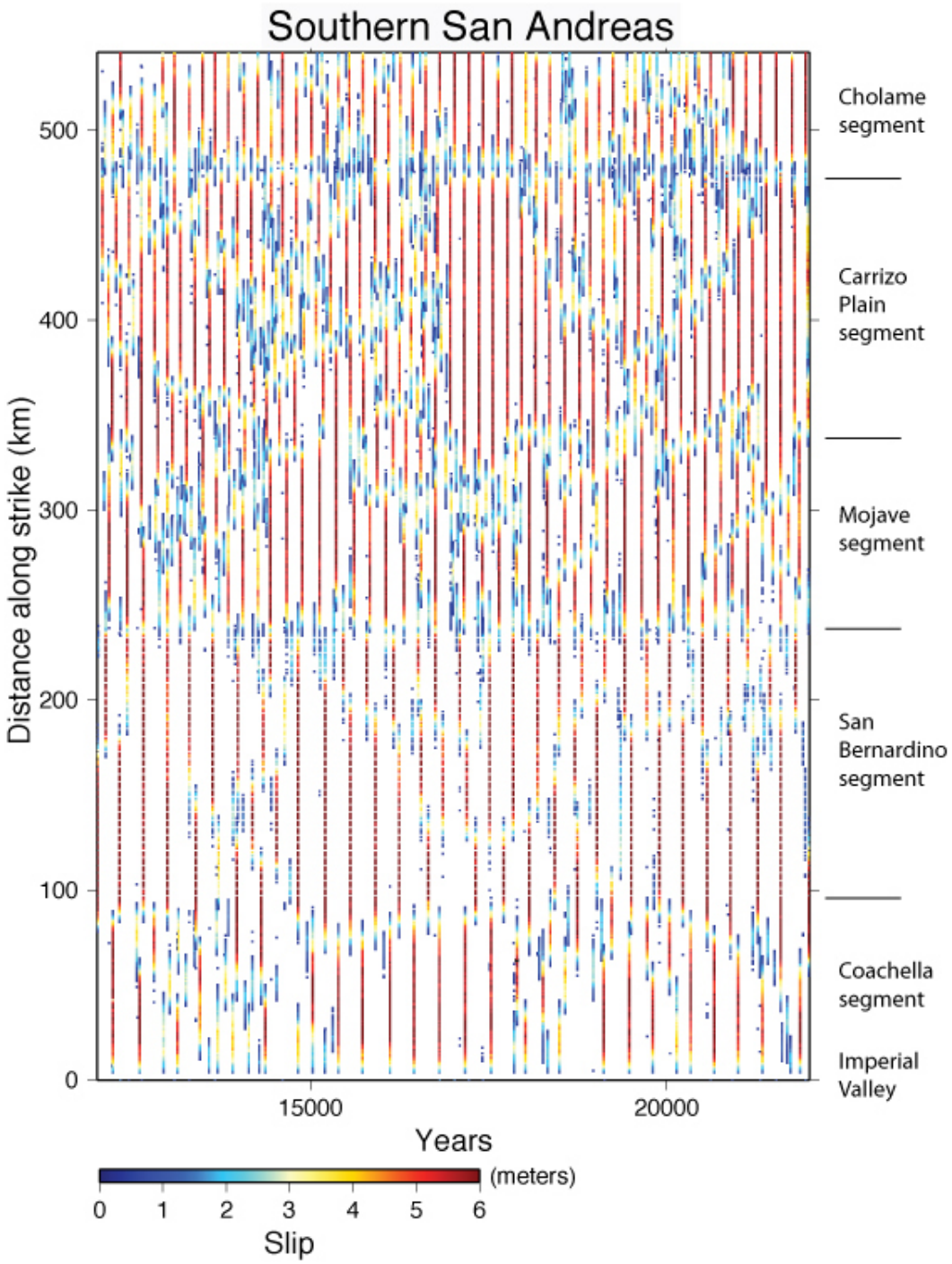

Figure 12: Slip map of the southern San Andreas fault for a 10000-year period, showing slip as a function of time and distance along strike, measured north from Imperial Valley, for all M $>$ 6.5 events. Simulation parameters are $\eta_m = 1.2 \times 10^{19}$ Pa s and $\gamma = 2$ MPa/m.

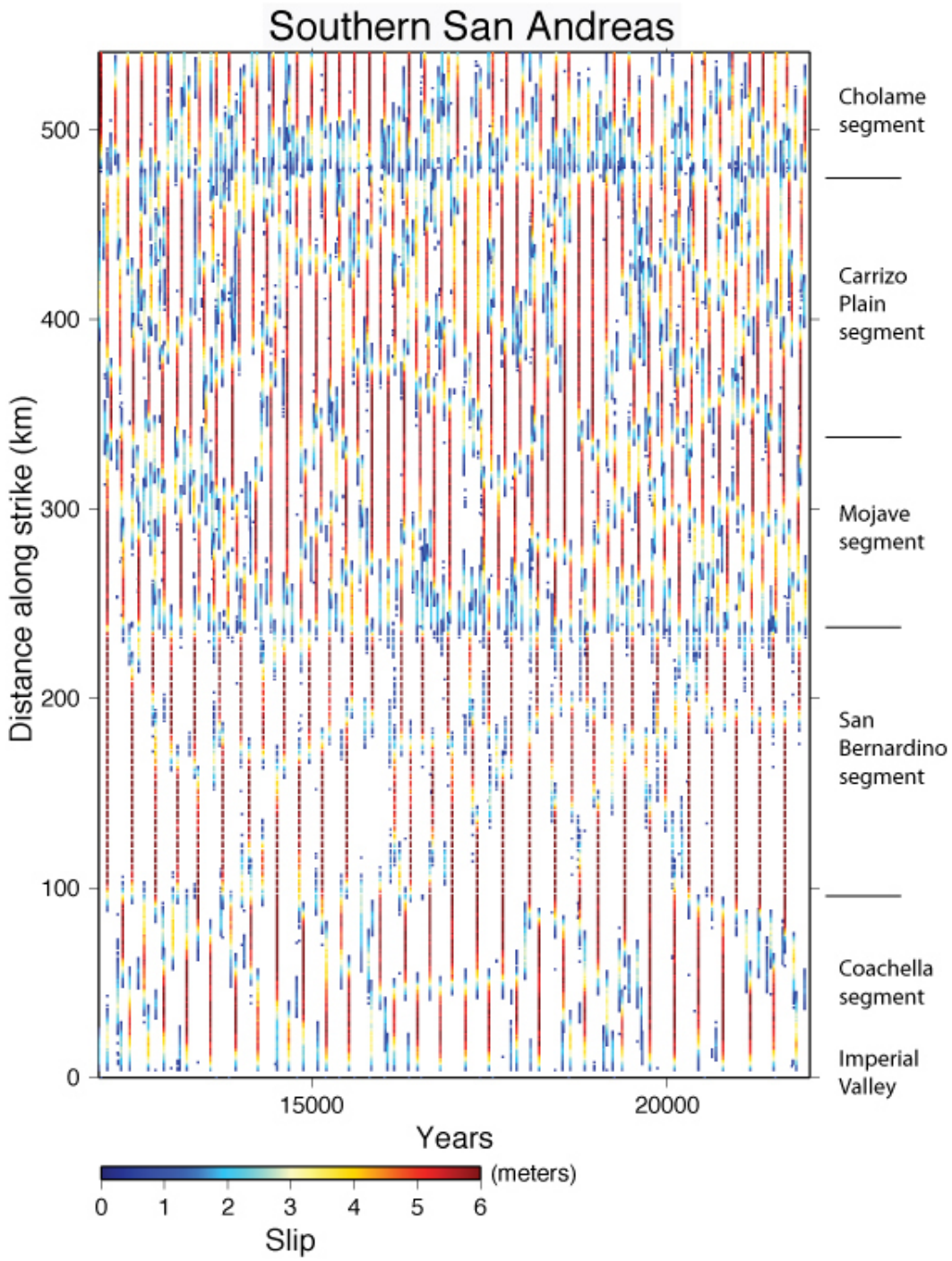

Figure 13: Slip map of the southern San Andreas fault for a 10000-year period, showing slip as a function of time and distance along strike, measured north from Imperial Valley, for all M $>$ 6.5 events. Simulation parameters are $\eta_m = 3 \times 10^{19}$ Pa s and $\gamma = 2$ MPa/m.

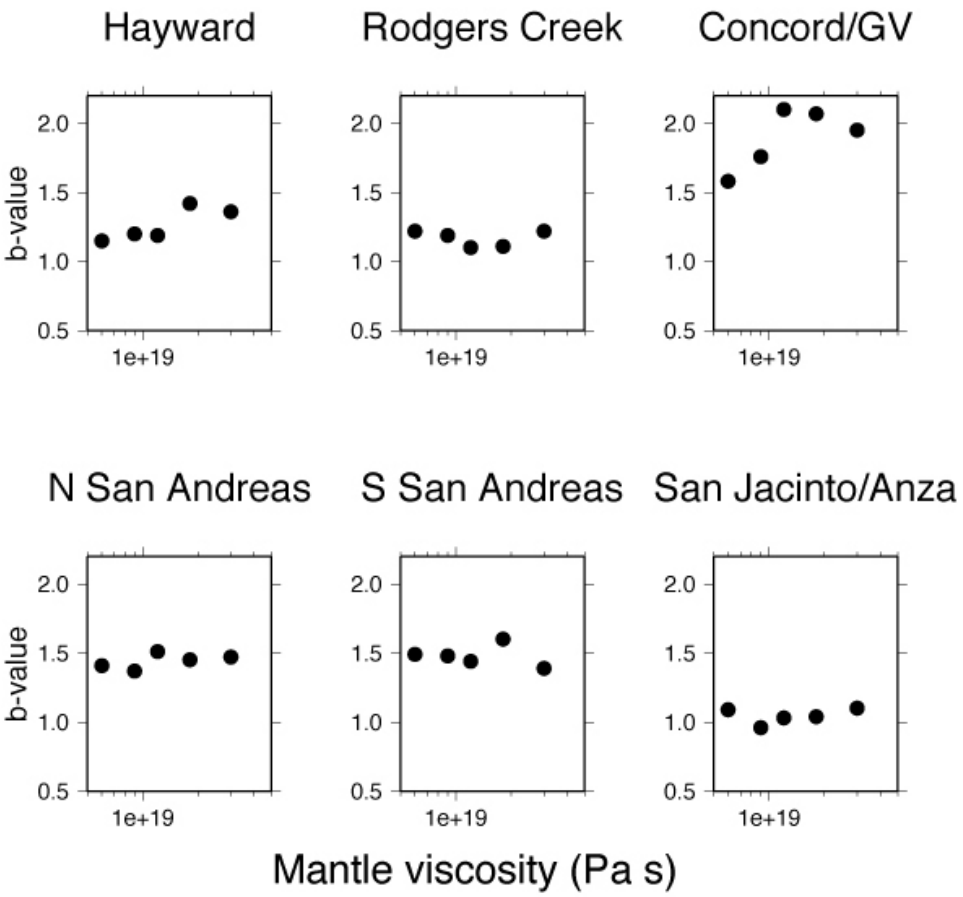

Figure 14: $b-$value obtained on given faults as a function of η_m for a simulation with $\gamma = 2$ MPa/m.

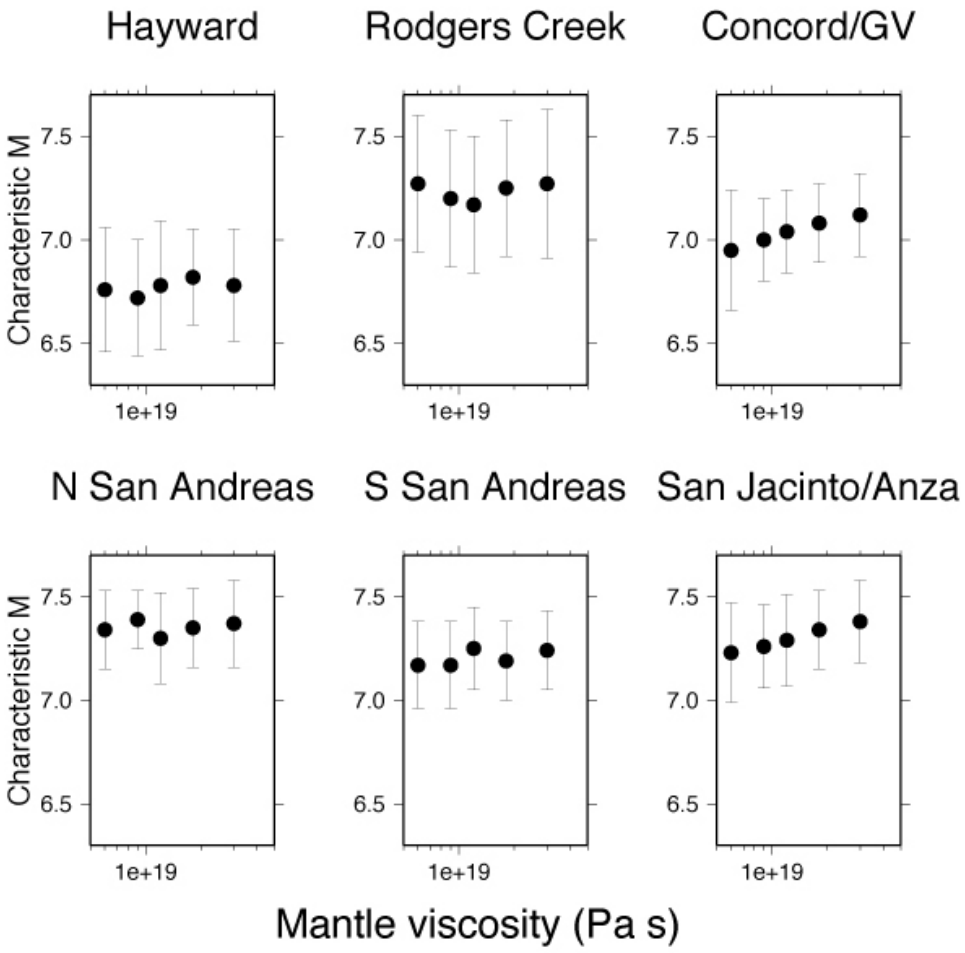

Figure 15: Characteristic magnitude obtained on given faults as a function of η_m for a simulation with $\gamma = 2$ MPa/m.

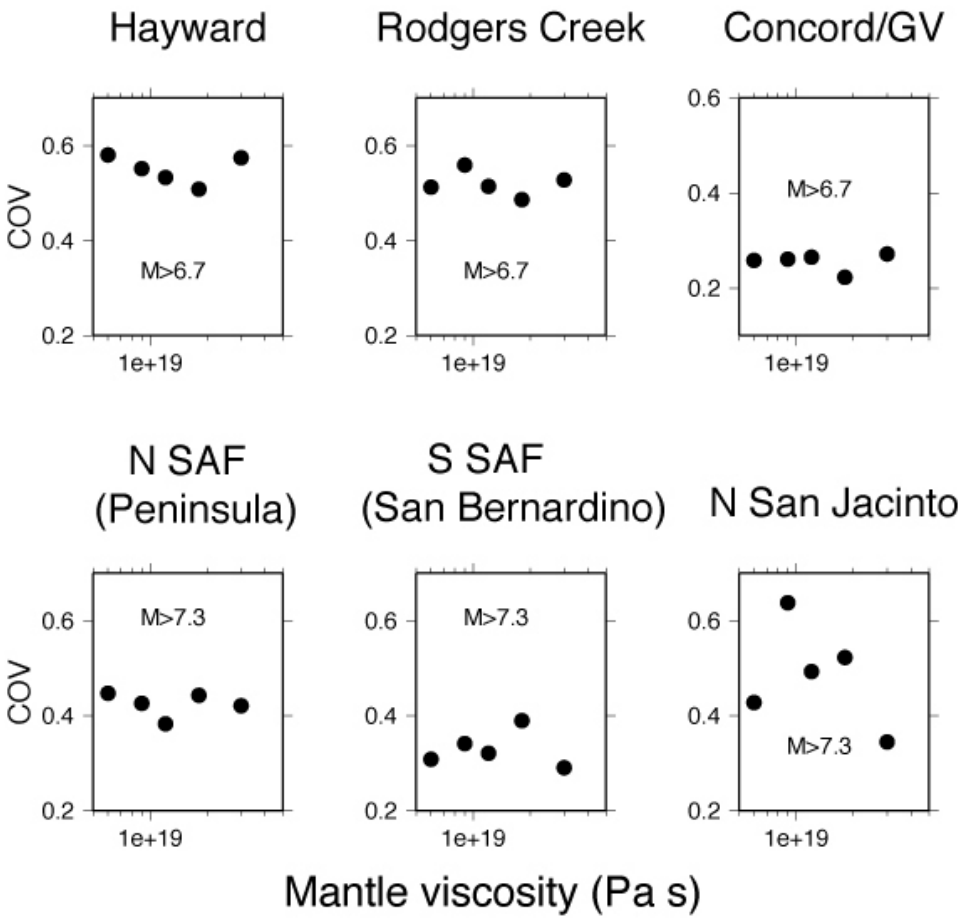

Figure 16: COV obtained on given faults, at the given magnitude thresholds, as a function of η_m for a simulation with $\gamma = 2$ MPa/m. Note that the larger faults are sampled only on specific segments or at a point (northern SAF Peninsula segment; southern SAF San Bernardino segment; northern San Jacinto fault at the point 33.9092°N 117.1122°W)

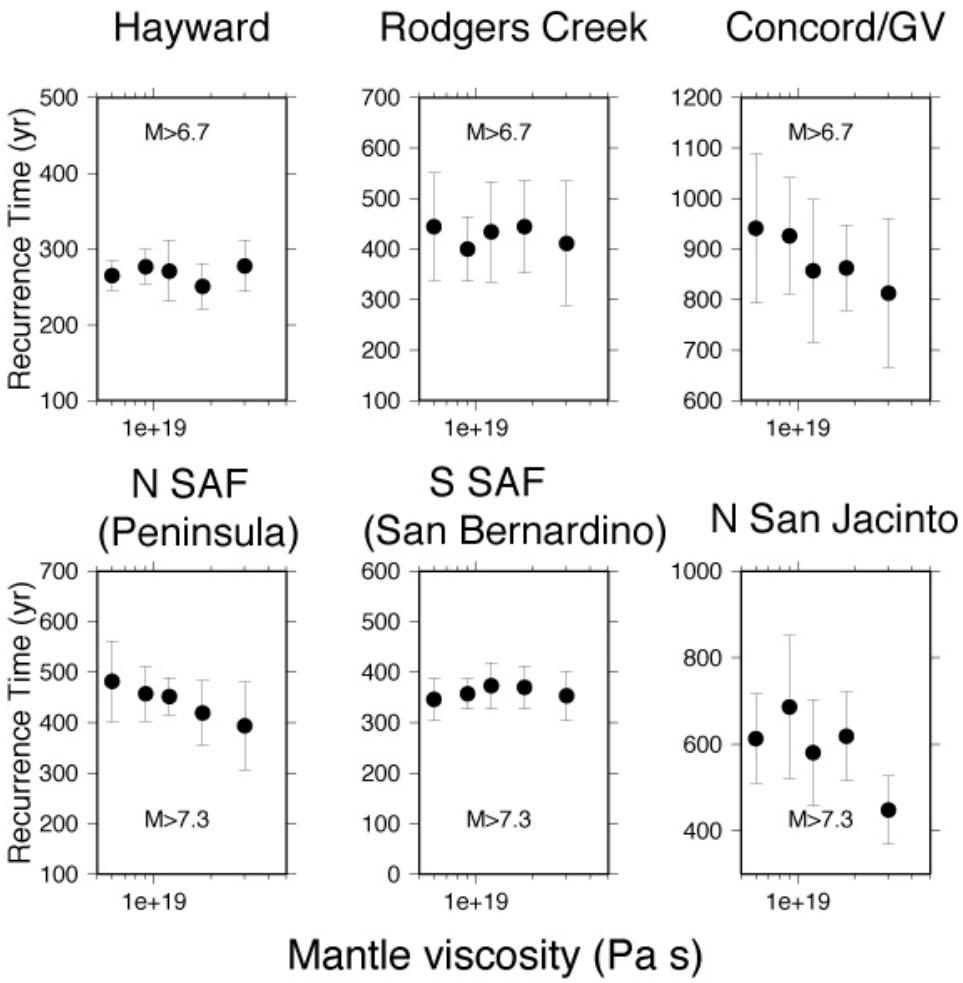

Figure 17: Mean recurrence interval T obtained on given faults, at the given magnitude thresholds, as a function of η_m for a simulation with $\gamma = 2$ MPa/m. Note that the larger faults are sampled only on specific segments or at a point (northern SAF Peninsula segment; southern SAF San Bernardino segment; northern San Jacinto fault at the point 33.9092°N 117.1122°W)

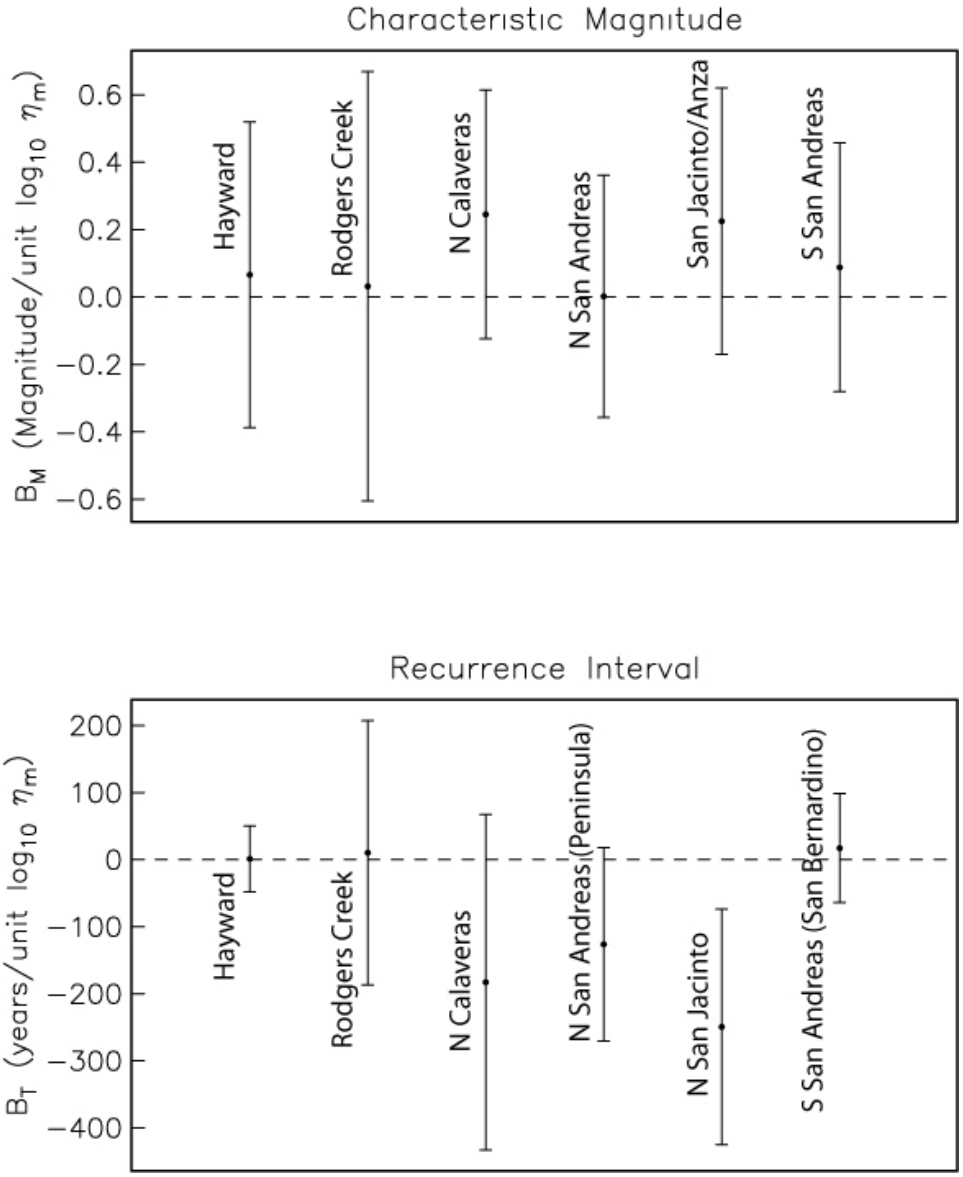

Figure 18: Slopes B_M and B_T resulting from fitting obtained M and T variations with viscosity (i.e. Figures 15 and 17) with linear fits in $\log_{10}\eta_m$ (eqn 2).